Iron oxide nanoparticles: tunable size synthesis and analysis in terms of core-shell structure and mixed coercive model

P. T. Phong[1,2], V. T. K. Oanh[3,4], T. D. Lam[4], N. X. Phuc[3], L. D. Tung[5,6,*], Nguyen T. K. Thanh[5,6], D. H. Manh[3,**]

[1]Department for Management of Science and Technology Development, Ton Duc Thang University, Ho Chi Minh City, Vietnam.

E-mail: phamthanhphong@tdt.edu.vn

[2]Faculty of Applied Sciences, Ton Duc Thang University, Ho Chi Minh City, Vietnam

[3]Institute of Materials Science, Vietnam Academy of Science and Technology, 18 Hoang Quoc Viet, Hanoi, Vietnam.

[4]Graduate University of Science and Technology, Vietnam Academy of Science and Technology, 18 Hoang Quoc Viet, Hanoi, Vietnam.

[5]Biophysics Group, Department of Physics and Astronomy, University College London, Gower Street, London, WC1E 6BT, UK.

[6]UCL Healthcare Biomagnetic and Nanomaterials Laboratories, 21 Albemarle Street, London W1S 4BS, UK

Corresponding author: D.H. Manh, Associate Professor of Institute of Materials Science, Vietnam Academy of Science and Technology

Email: manhdh.ims@gmail.com. Tel: +84 43836 4403; Fax: +84 43836 0705.

Co-corresponding author: L.D. Tung, Dr. of Department of Physics and Astronomy, University College London

Email: t.le@ucl.ac.uk

ABSTRACT: Iron oxide nanoparticles (NPs) are currently a very active research field. To date, a comprehensive study on iron oxide NPs is still lacking not only on the size dependence of structural phases but also the use of appropriate model. Herein, we report on a systematic study of the structural and magnetic properties of iron oxide NPs prepared by a co-precipitation method followed by hydrothermal treatment. X-ray diffraction and transmission electron microscopy reveal that the NPs have an inverse spinel structure of iron oxide phase (Fe_3O_4) with average crystallite sizes (D_{XRD}) of 6 - 19 nm, while grain sizes (D_{TEM}) of 7 - 23 nm. In addition, the larger the particle size, the closer the experimental lattice constant value to that of the magnetite structure. Magnetic field-dependent magnetization data and analysis show that the effective anisotropy constants of the Fe_3O_4 NPs are about 5 times larger than that of its bulk counterpart. Particle size (D) dependence of the magnetization and the non-saturating behavior observed in applied fields up to 50 kOe are discussed using the core-shell structure model. We find that with decreasing D, while the calculated thickness of the shell of disordered spins ($t \sim$ 0.3 nm) remains almost unchanged, the specific surface areas S_a increases significantly, thus reducing the magnetization of the NPs. We also probe the coercivity of the NPs by using the mixed coercive Kneller and Luborsky model. The calculated results indicate that the coercivity rises monotonously with the particle size, and are well matched with the experiment ones.

Keyword: Iron oxide; hydrothermal; effective anisotropy; coercive force; magnetization.

1. Introduction

Over the last decade magnetic nanomaterials are of considerable scientific interest due to the possibilities they offer in a broad range of applications in economy, energy efficiency, homeland security, and defense [1]. Among these magnetic materials, iron oxide nanoparticles (NPs) have been attracting much research attention owing to their remarkable properties that appear at nanometer scale as well as their great potential applications in environmental engineering, mechano-electrical fields, microfluid and biomedicine [2, 3].

It is known that, because of the small size, NPs can show some special features different to their bulk counterpart such as superparamagnetic behavior, exchange bias, spin-glass, and there is a complex interplay between surface effects, finite size effects, and inter-particle interactions [4-6]. The effects of surface on the behaviors of NPs have often been explained by a core-shell model [7-9] of which the core of the particle would have some features similar to its bulk counterpart, such as saturation magnetization and intrinsic magnetocrytalline anisotropy. On the other hand, the shell would have defects in crystallographic structure, which lead to a magnetically dead layer with the thickness supposedly increasing with decreasing particle size [10-12].

The anisotropy of magnetic NPs arises from different sources, including magnetocrystalline, surface, shape, and strain anisotropies. For magnetic NPs, the observed coercivity can be affected by different causes including internal stress, contamination, surface irregularities, shape and particle size. The coercivity variation with temperature is explained from the accurate measurement of the effective magnetic anisotropy (K_{eff}). Since K_{eff} of NPs cannot be measured directly by magnetotorquemeter, the law of approach to saturation has been applied to calculate K_{eff} of NPs [13].

Although there are a lot of articles reported on the evolution of the structural and magnetic property of iron oxide nanoparticles as a function of the size [14-17], until now, a detailed analysis on the size dependence of the Fe_3O_4 and γ-Fe_2O_3 phases by using the x-ray diffraction (XRD) data or of the coercivity by using the mixed coercive model has yet to be reported. Here, we report on a detailed study of the structural and magnetic properties of iron oxide NPs prepared by a co-precipitation method followed by hydrothermal treatment. The aim is to find out the size dependence of magnetization, coercivity, magnetic anisotropy of the synthesized NPs as well as the effects of specific surface area (S_a) on the saturation magnetization and the effective anisotropy constants. The observed coercivity of the NPs is discussed in terms of the mixed coercive Kneller and Luborsky model [13, 18].

2. Experimental

Synthesis of iron oxide NPs by hydrothermal method

The chemical reagents used in this work were ferrous chloride tetrahydrate ($FeCl_2.4H_2O$), ferric chloride hexahydrate ($FeCl_3.6H_2O$), sodium hydroxide (NaOH), and hydrochloric acid (HCl). All chemicals, obtained from Sigma–Aldrich Ltd (Singapore), are of analytical grade and to be used without any further purification.

$FeCl_2.4H_2O$ (19.9 g) and $FeCl_3.6H_2O$ (16.22 g) were dissolved in 50 mL of 2 M HCl acid separately before the reaction to ensure that they are completely dissolved when they are mixed together. A prepared solution of 2 ml Fe^{2+} and 4 ml Fe^{3+} was mixed in a 100 mL flask and being stirred by a mechanical stirrer under nitrogen flow to ensure inert atmosphere. Then, 80 mL of 2M NaOH was gradually dropped into the mixture and precipitate iron oxide NPs seed can be seen to begin forming. The mixture was then immediately transferred into a 100 mL Teflon-lined stainless steel autoclave vessel that was put in an oven and heated for 2 hrs in the temperature range of 100 – 180 ^oC and cooled naturally to room temperature. The product was isolated by applying a permanent magnet and washed four to five times with distilled water (until pH = 7) to

eliminate unwanted impurities. Finally, the precipitated powders were dried and labeled S1, S2, S3, S4, and S5 corresponding to the heated temperatures of 100, 120, 140, 160 and 180 ^{o}C, respectively. The reaction was repeated three times and we obtained reproducible results. Our synthesis procedure is similar to that reported in ref. [19].

Characterization of iron oxide NPs

The structural characterizations were investigated with a SIEMENS D5000 diffractometer using Cu-Kα radiation at wave length λ = 1.5406 Å. The diffraction patterns were collected with 2θ in the range of 20° - 70°. The morphology, particle size, and size distribution of the NPs were examined with a JEOL JEM-1010 transmission electron microscope (TEM) operated at an acceleration voltage of 80 kV.

The magnetic measurements were carried out on non-diluted dried powder sample. Field-dependent magnetization M (H) of the samples was measured at 300 and 5 K with applied fields up to 50 kOe using a Quantum design hybrid superconducting quantum interference device-vibrating sample magnetometer (SQUID-VSM).

3. Results and discussion

Structural characterization

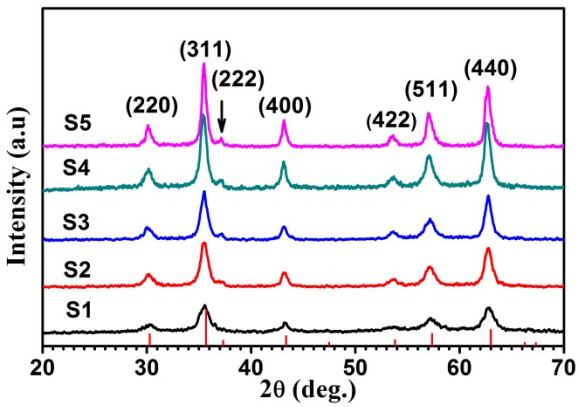

Fig. 1. X-ray patterns of all the samples synthesized at various heated temperatures along with the reference pattern of Fe_3O_4.

Room temperature X-ray diffraction (XRD) patterns of the samples synthesized at various temperatures are represented in Figure 1. It can be seen that the diffraction peaks for all samples can be indexed to (220), (311), (222), (400), (422), (511) and (440) of an inverse spinel structure. However, since the diffraction peaks of maghemite (γ-Fe_2O_3) and magnetite (Fe_3O_4) structures are similar to each other, it was not possible to distinguish conclusively whether the patterns belonging to either phase [20].

To better evaluate the available crystal phases in the samples we have also determined the experimental lattice constant (a_{exp}) by using the following relationship:

$$a_{exp} = d_{hkl}\sqrt{h^2 + k^2 + l^2} \quad (1)$$

where (h k l) are the Miller indices and d_{hkl} the inter-planar spacing obtained from Rietveld analysis. The obtained a_{exp} values of the samples varied from 8.367 Å to 8.391 Å (see Table 1), which are larger than that of the bulk maghemite (8.346 Å) and smaller than that of the bulk magnetite (8.396 Å) [19]. Here the larger the particle size, the closer the calculated a_{exp} value to that of the magnetite structure.

Table 1. Inter-planar spacing (d_{hkl}), experimental lattice parameter (a_{exp}), X-ray density (ρ_x), thickness of the surface layer (t), specific surface area (S_a) and average crystallite sizes (D_{XRD}) of iron oxide samples prepared at various heated temperatures (T)

Sample	T (^oC)	d_{hkl} (Å)	a_{exp} (Å)	ρ_x (g/cm^3)	t (nm)	S_a (m^2/g^1)	D_{XRD} (nm)
S1	100	2.523	8.367	5.2511	0.30	228.5	5.8
S2	120	2.523	8.367	5.2511	0.34	163.2	7.6
S3	140	2.526	8.378	5.2306	0.43	143.4	10.8
S4	160	2.527	8.381	5.2250	0.44	114.8	12.9
S5	180	2.530	8.391	5.2063	0.46	76.8	19.5

The changing trend of the Fe_3O_4 and γ-Fe_2O_3 phases in the iron oxide nanoparticles is consistent with those previously reported by [21] in which the iron oxide phases were determined by innovative synchrotron X-ray total scattering methods and Debye function analysis.

To quantify the size effects on the lattice constant, we have also calculated the theoretical lattice constant (a_{th}) through expression [22]:

$$a_{th} = \frac{8}{3\sqrt{3}}\left[(r_A + R_O) + \sqrt{3}(r_B + R_O)\right] \quad (2)$$

where R_O = 1.32 Å is the radius of the oxygen, r_A and r_B the radii of Fe^{2+} and Fe^{3+}, respectively. The obtained a_{th} (8.445 Å) is larger than both the bulk and NPs samples. The cause of the decline of the lattice constant of the NPs is probably related to the fact that some ferrous ions Fe^{2+} with large radius ($r_{Fe^{2+}}$ = 0.78 Å) were oxidized to Fe^{3+} with smaller radius ($r_{Fe^{3+}}$ = 0.645 Å) and formed γ-Fe_2O_3 on the surface of the NPs [19, 23].

The average crystallite size (D_{XRD}) was calculated by the Debye-Scherrer method [24] using the following equation:

$$D_{XRD} = \frac{0.89\lambda}{\beta cos\theta} \quad (3)$$

where λ = 0.1546 nm is the wavelength of the X-ray radiation, θ Bragg's angle and β the full width at half maximum of the (311) peak. The obtained values D presented in Table 1 show an increase of D with the heated temperatures.

The specific surface area (S_a) can be determined by: $S_a = 6/\rho_X D$, in which the X-ray density (ρ_x) deduced from following relation [25],

$$\rho_X = \frac{8M}{Na^3} \quad (4)$$

where M is molecular weight and N Avogadro's number. The ρ_x and S_a values of the samples are also presented in Table 1 and they decrease as D increases.

TEM images of two typical samples S1 and S5 are presented in Figure 2 that shows the presence of spherical and near-cubic NPs. A manual statistical count of grain size has been performed on TEM images using the Image-J software. Particle size distributions were obtained from measurement of at least 125 particles per sample are presented in Figures 2b and 2d which show these distribution according to a Lorentzian law. We obtained the average diameter D_{TEM} of S1 and S5 samples of 7 nm and 22 nm, respectively. These values are very close with those of the crystallite sizes determined previously by Scherer formula from the X-ray patterns as can be seen in Table 1.

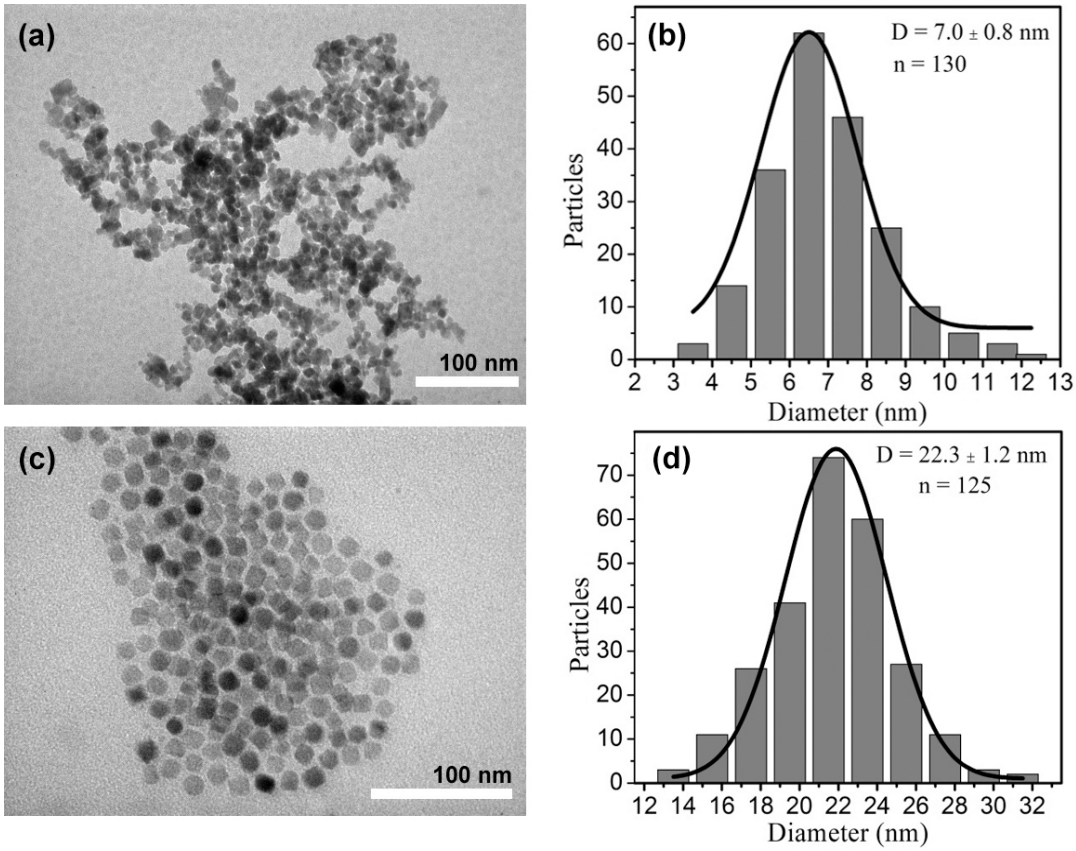

Fig. 2. TEM photographs (a, c) and particle size distributions (b, d) of two typical samples S1 and S5. Size distributions were obtained from the measurement of at least 125 particles per sample (n) and were fitted with a normal log function (solid line).

Magnetic characterizations

Figure 3 presents the hysteresis (M-H) loops for all samples at 5 and 300 K. At 5 K and 300 K, using the law of approach to saturation (Eq. 6), the values of saturation magnetization

(M_s) are obtained in between 75-89 emu/g and 64-80 emu/g, respectively. The values of M_s, coercivity (H_c), remanence (M_r) and squareness ratio ($SR = M_r/M_s$) of all samples are listed in Table 2. For the cube NPs (S5), the *SR* and H_c are consistent with those previously reported for Fe_3O_4 NPs [5]. The presence of small squareness ratios in the hysteresis loops for all samples even at 5K indicates either the presence of a mixture of blocked and superparamagnetic nanoparticles (i.e. mixed coercive model) or this could also be attributed to deviations from a uniaxial anisotropy and to the effect of interparticle interactions. We did not find the presence of Vervey transition from the temperature dependence of the magnetization measurement M(T) (not shown here). Goya et al [15] reported that this transition could be observed in magnetite nanoparticles of 50 and 150 nm rather than 5 and 10 nm prepared by different chemical techniques. However, the Verwey transition was tracked by variable-temperature scanning tunneling microscopy in individual ~10 nm magnetite nanocrystals prepared by the coprecipitation technique and embedded in the surface of a gold film [26]. Thus, this transition is dependent on size as well as measuring and preparing methods.

The effects of surface to the magnetic property of NPs are often explained by a core-shell model, where the core of the particle should have the same saturation magnetization and intrinsic magnetocrystalline anisotropy as its bulk counterpart, while the shell with thickness *t* may be considered as a highly disordered magnetic system due to high surface energy or pinning of the surface spins [27]. In order to gain further insight into the core-shell structure, the thickness of the surface layer (*t*) of the particle was determined by using the following expression,

$$M_s = M_s(\infty)\left(1 - \frac{6t}{D}\right) \quad (5)$$

If we assume $M_s(\infty)$ = 92 emu/g, i.e. the bulk value of Fe_3O_4 at room temperature, from the values of *D* and M_s listed in Table 1, the value of *t* varies from 0.3 to 0.4 nm (see Table 1), which is in good agreement with that reported by Chen *et al.* [28].

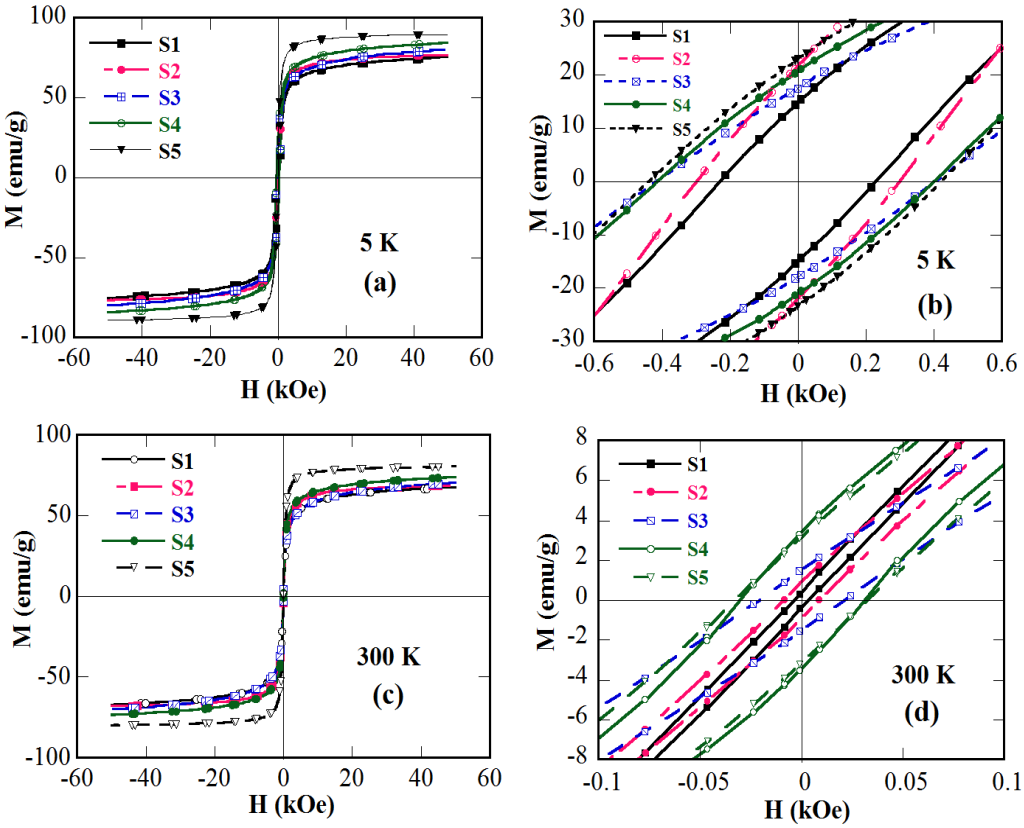

Fig. 3. Hysteresis loops (left) and the zoom-in view around the origin (right) for all samples at 5 K (a, b) and 300 K (c, d).

The relation between M_s and S_a for all the samples at 5 K and 300 K is presented in Figure 4. It can be seen that M_s decreases but S_a increases with decreasing D while the calculated thickness of the surface layer t remains almost unchanged. As a result, the contribution of the non-magnetic surface layer would increase, resulting in a decrease in the total M_s. Our result is similar to those reported previously by Yang *et al.* [14] and it appears that the core-shell structure model for iron oxide NPs could explain well for the size dependence of magnetization and the non-saturating behavior of the samples in a high field of 50 kOe.

In order to determine the magnetic anisotropies of the magnetic NPs we used the law of approach to saturation well below T_c, which can be written as [29]:

$$M(H) = M_s\left(1 - \frac{a}{H} - \frac{b}{H^2} - \cdots\right) + \chi_d H \qquad (6)$$

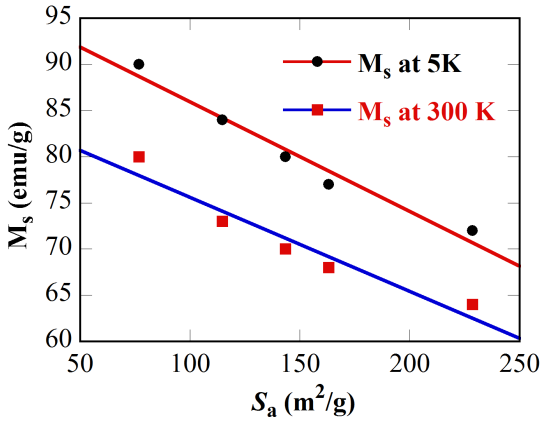

Fig. 4. Saturation magnetization versus the specific surface area at 5 K and 300 K for the samples.

where M_s and χ_d are the saturation magnetization at a particular temperature and the high field susceptibility, respectively. The b/H^2 term has its origin in various types of magnetic anisotropies such as magnetocrystalline and effective (shape and strain) anisotropies. Assuming that the particles are randomly oriented and if the strain anisotropy for the magnetite NPs is excluded, K_{eff} can be obtained [14] as follows:

$$b = \frac{1}{M_s^2}\left(\frac{8}{105}K_1^2 + \frac{4}{15}K_{eff}^2\right) \quad (7)$$

where K_1 and K_{eff} are the magnetocrystalline and effective anisotropy constants, respectively. For all samples in the calculation, we assume the crystalline anisotropy constant K_1 to be the same as that of the bulk magnetite of 1.35×10^5 erg/cm^3 [3] and the calculated values of K_{eff} are listed in Table 2. It can be seen that the values of K_{eff} are almost equivalent to each other and about 5 times larger than that of bulk magnetite.

The coercivity for a randomly oriented single domain particles (i.e. $SR \leq 0.5$) could be explained by the mixed coercive model of Kneller and Luborsky [14]. For NPs, there is a difference between critical values for single domain size and that of the superparamagnetic one. In case of magnetite particles, the corresponding values are of 128 nm [30] and 17 nm [31],

respectively.

Table 2. Saturation magnetization (M_s), effective anisotropy constant (K_{eff}), squareness ratio (SR), experimental coercivity (H_c), and theoretical coercivity (H_c^{th}) of samples S1- S5 obtained at 5 K and 300 K

Sample	T (K)	M_s (emu/g)	K_{eff} (10^5erg/cm^3)	SR	H_c (Oe)	H_c^{th} (Oe)
S1	5	75	26.71	0.18	221.5	228.7
	300	64	7.62	0.01	2.3	2.3
S2	5	76	26.39	0.20	294.7	274.3
	300	67	7.59	0.02	7.6	7.0
S3	5	80	26.18	0.24	405.7	353.9
	300	70	7.53	0.04	15.7	13.7
S4	5	84	24.94	0.26	406.9	387.2
	300	73	7.49	0.07	27.5	23.0
S5	5	89	24.69	0.27	415.6	395.2
	300	80	7.19	0.09	32.2	26.8

For randomly oriented superparamagnetic particles, the volume percentage of single domain particles is $x = M_r/(0.5M_s)$ and according to the Kneller and Luborsky model, the average coercivity of a mixture of superparamagnetic and single domain particles is [14]:

$$\overline{H_C} = \frac{H_C}{1+\frac{H_C\, yV_sM_s}{0.5x\ 3k_BT}} \tag{8}$$

where y is the volume percentage of superparamagnetic particles, k_B the Boltzmann constant, $H_c = 0.96K/M_s$, K the total magnetic anisotropy constant at a certain temperature ($K = K_1 + K_{eff}$) and the volume V_s of NP can be deduced from the formula $25k_BT = K_{eff}V$ [32].

With the known values of M_s, SR, V_s, and K, the corresponding theoretical coercivity, H_c^{th}, can be calculated and its values are listed in Table 2. It can be seen that the calculated values of H_c^{th} of all the samples are consistent with those derived from the experiments pointing to the fact that the coercivity of the iron oxide NPs can be explained by homogeneous rotation mechanism.

4. Conclusions

In summary, we have successfully synthesized iron oxide NPs by hydrothermal method with controllable mean crystallite sizes in the range of 6 - 19 nm. The largest NPs of 19 nm have the highest saturation magnetization of 80 emu/g at 300 K. The NPs possess a smaller saturation magnetization, but a higher effective anisotropy comparable with the bulk sample of Fe_3O_4 phase. The size dependence of the magnetization and the non-saturating behavior of the samples up to the applied field of 50 kOe are consistent with the picture of the core-shell structure. We have also indicated that the mixed coercive model could be applied to predict the coercivity for the NPs.

Acknowledgments

This research was funded by Vietnam National Foundation for Science and Technology (NAFOSTED) under grant number 103.02-2015.74 and funded by the AOSRD award FA 2386 14-1-0025. Nguyen T.K. Thanh thanks EPRSC for financial support.

References

[1] S.D. Bader, Rev. Mod. Phys. 78, 1 (2006).

[2] Q.A. Pankhurst, J. Connolly, S.K. Jones, J. Dobson, J. Phys. D: Appl. Phys. 36, R167 (2003).

[3] G.F. Goya, T.S. Berquo, F.C. Fonseca, and M.P. Morales, J. Appl. Phys. 94, 3520 (2003).

[4] L. Wang, J. Luo, Q. Fan, M. Suzuki, I.S. Suzuki, M.H. Engelhard, Y. Lin, N. Kim, J.Q. Wang, C.J. Zhong, J. Phys. Chem. B 109, 21593 (2005).

[5] H. Khurshid, J. Alonso, Z. Nemati, M.H. Phan, P. Mukherjee, M.L. Fdez-Gubieda, J.M. Barandiarán, and H. Srikanth, J. Appl. Phys. 117, 17A337 (2015).

[6] M. Suzuki, S.I. Fullem, I.S. Suzuki, L. Wang, C.J. Zhong, Phys. Rev. B 79, 024418 (2009).

[7] B. Martínez, X. Obradors, L. Balcells, A.Rouanet, C.Monty, Phys. Rev. Lett. 80, 181 (1998).

[8] M.H. Phan, J. Alonso, H. Khurshid, P.L. Kelley, S. Chandra, K.S. Repa, Z. Nemati, R. Das, O. Iglesias, H. Srikanth, Nanomaterials (2016) doi: 10.3390/nano6110221.

[9] Y. Hwang, S. Angappane, J. Park, K. An, T. Hyeon, J.G. Park, Curr. Appl. Phys. 12, 808 (2012).

[10] Q.K. Ong, A. Wei, X.M. Lin, Phys. Rev. B 80, 134418 (2009).

[11] D.H. Manh, P.T. Phong, T.D. Thanh, D.N.H. Nam, L.V Hong, N.X Phuc, J. Alloy. Compd. 509, 1373 (2011).

[12] S. Gangopadhyay, G.C. Hadjipanayis, B. Dale, C.M. Sorensen, K.J. Klabunde, V. Papaefthymiou and A. Kostikas, Phys. Rev. B 45, 9778 (1992).

[13] E.F. Kneller and F.E. Luborsky, J. Appl. Phys. 34, 656 (1963).

[14] K. Woo, J. Hong, S. Choi, H.W. Lee, J.P. Ahn, C.S. Kim, S.W. Lee, Chem. Mater. 16, 2814 (2004).

[15] G.F. Goya, T.S. Berquo, and F.C. Fonseca, J. Appl. Phys. 94, 3520 (2003).

[16] Jaime Santoyo Salazar, Lucas Perez, Oscar de Abril, Lai Truong Phuoc, Dris Ihiawakrim, Manuel Vazquez, Jean-Marc Greneche, Sylvie Begin-Colinand, Genevieve Pourroy, Chem. Mater. 23, 1379 (2011).

[17] A.G. Roca, M.P. Morales, K. O'Grady and C.J. Serna, Nanotechnology 17, 2783 (2006).

[18] J. P. Wang, D.H. Han, H. L. Luo, Q.X. Lu, Y.-W. Sun, Appl. Phys. A 61, 407 (1995).

[19] G.M. Costa, C. Blanco-Andujar, E.D. Grave and Q.A. Pankhurst, J. Phys. Chem. B 118, 11738 (2014).

[20] T. Ozkaya, M.S. Toprak, A. Baykal, H. Kavas, Y. Köseoğlu, B. Aktaş, J. Alloy. Compd. 472, 18 (2009).

[21] R. Frison, G. Cernuto, A. Cervellino, O. Zaharko, G.M. Colonna, A. Guagliardi, N. Masciocchi, Chem. Mater. 25, 4820 (2013).

[22] S.A. Mazen, M.H. Abbdallah, B.A. Sabrah, H.A.M. Hasham, Phys. Status Solidi A 134, 263 (1992).

[23] T.J. Daou, G. Pourroy, S. Begin-Colin, J.M. Greneche, C. Ulhaq-Bouillet, P. Legare, P. Bernhardt, C. Leuvrey, G. Rogez, Chem. Mater. 18, 4399 (2006).

[24] Triloki, P. Garg, R. Rai, B.K. Singh, Nucl. Instrum. Methods Phys. Res. A 736, 128 (2014).

[25] P.T. Phong, P.H. Nam, D.H. Manh, D.K. Tung, I.J. Lee, N.X. Phuc, J. Electron. Mater. 44, 287 (2015).

[26] A. Hevroni, M. Bapna, S. Piotrowski, S.A. Majetich, and G. Markovich, J. Phys. Chem. Lett. 7, 1661 (2016).

[27] K. Parekh and R.V. Upadhyay, J. Appl. Phys. 107, 053907 (2010).

[28] J.P. Chen, C.M. Sorensen, K.J. Klabune, G.C. Hadjipanayis, E. Devlin, A. Kostikas, Phys. Rev. B 54, 9288 (1996).

[29] D.K. Tung, D.H. Manh, P.T. Phong, L.T.H. Phong, N.V. Dai, D.N.H. Nam, N.X. Phuc, J. Alloy. Compd. 640, 34 (2015).

[30] C. Kittel, Phys. Rev. 70, 965 (1946).

[31] G. Sun, Mikhail Y. Berezin, J. Fan, H. Lee, J. Ma, K. Zhang, K.L. Wooley, S. Achilefu, Nanoscale 2, 548 (2010).

[32] N. Jovic, B. Antic, G.F. Goya, and V. Spasojevic, Curr. Nanosci. 8, 651 (2012).

Fig. 1. X-ray patterns of all the samples synthesized at various heated temperatures along with

the reference pattern of Fe_3O_4.

Fig. 2. TEM photographs (a, c) and particle size distributions (b, d) of two typical samples S1 and S5. Size distributions were obtained from the measurement of at least 125 particles per sample (n) and were fitted with a normal log function (solid line).

Fig. 3. Hysteresis loops (left) and the zoom-in view around the origin (right) for all samples at 5 K (a, b) and 300 K (c, d).

Fig. 4. Saturation magnetization versus the specific surface area at 5 K and 300 K for the samples.